UNIVERSITY *of* York

This is a repository copy of *The nanoscale molecular chemistry of outer solar system organic matter in asteroid Ryugu*.

White Rose Research Online URL for this paper:
https://eprints.whiterose.ac.uk/id/eprint/230825/

White Rose
university consortium
Universities of Leeds, Sheffield & York

eprints@whiterose.ac.uk
https://eprints.whiterose.ac.uk/

The nanoscale molecular chemistry of outer solar system organic matter in asteroid Ryugu

Christian Vollmer[1], Demie Kepaptsoglou[2,3], Johannes Lier[1], Aleksander B. Mosberg[2], and Quentin M. Ramasse[2,4]*

[1]Institut für Mineralogie, Universität Münster, Corrensstr. 24, 48149 Münster, Germany. *corresponding author

[2]SuperSTEM Laboratory, Keckwick Lane, Daresbury, UK

[3]School of Physics, Engineering and Technology, University of York, Heslington, YO10 5DD, UK

[4]School of Chemical and Process Engineering and School of Physics and Astronomy, University of Leeds, Leeds LS2 9JT, UK

Email addresses:

christian.vollmer@uni-muenster.de

*corresponding author, ORCID ID: 0000-0002-7768-7651

dmkepap@superstem.org

qmramasse@superstem.org

abmosberg@superstem.org

jlier@uni-muenster.de

Submitted on June 16 2025

Abstract

The analysis of biorelevant molecules in returned mission samples such as from the carbonaceous asteroid (162173) Ryugu is key to unravelling the role of extraterrestrial organics in the evolution of life. Coordinated analyses using minimally destructive techniques at the finest length-scales on pristine samples are particularly important. Here, we identify the chemical signature of unique globular and nitrogen-containing diffuse organic matter in asteroid Ryugu and map the distribution of these biorelevant molecules with unprecedented detail. Using a novel electron-microscopy-based combination of vibrational and core-level spectroscopy, we disentangle the chemistry and nanoscale petrography of these organics. We show that some of these organics contain soluble and highly aliphatic components as well as NH_x functional groups, that must have formed in outer solar nebula environments before parent body incorporation. These novel coordinated analyses will open up new avenues of research on these types of precious and rare asteroidal dust samples.

Introduction

The Hayabusa2 mission by the Japan Aerospace Exploration Agency (JAXA) returned about 5.4 g from the Cb-type asteroid (162173) Ryugu to Earth on December 6th 2020[1]. Because these samples were immediately stored under controlled conditions after retrieval, terrestrial alteration is practically absent[2]. The spacecraft probed the regolith at two different locations, with chamber A material mainly from the surface and chamber C samples from regions deeper into the regolith. Early analyses show that Ryugu samples are very similar to Ivuna-type (CI) chondrites[2-5]. One of the major mission goals is to investigate the composition of organic matter (OM) and its relationship to matrix minerals such as phyllosilicates. OM in extraterrestrial samples comprises small soluble ("SOM") and large insoluble ("IOM") molecules that evolve in diverse circumstellar, interstellar and asteroidal environments and might play an important role for early biomolecule evolution on Earth[6-11].

Previous investigations of OM in extraterrestrial samples and specifically in Ryugu grains have demonstrated the extreme nanoscale heterogeneity of this material[12,13]. This complex makeup can be traced back to different evolutionary processes such as interstellar or nebular irradiation or parent-body fluid reactions, but it is generally highly challenging to disentangle these formation steps. OM can be analyzed non-destructively by infrared (IR) spectroscopy, for example, with the "MicrOmega" hyperspectral microscope[14,15] or atomic force microscopy (AFM) / Nano - IR setups[16-20]. The spatial resolution of these techniques is still limited at best to several tens of nanometers, which leads to gaps in our understanding of the fine-scale heterogeneity of this material and therefore its likely origins and evolution. We therefore need to combine novel high-spatial resolution techniques for these types of extremely fine-grained complex materials.

Here we reveal the molecular constitution and local, sub-nanometre heterogeneity of OM unique to Ryugu using high-energy-and-spatial resolution vibrational electron energy loss spectroscopy ("VibEELS") on minimally processed samples in a monochromated aberration-corrected Scanning Transmission Electron Microscope (STEM). We combine VibEELS, which measures the ultra-low ($\sim$0.05 – 0.5 eV) energy loss of electrons traversing the samples, with high spatial resolution imaging and core-level energy-loss near-edge fine structure (ELNES) analyses in the same areas. VibEELS has only recently become possible thanks to advanced monochromator designs for electron microscopes[21]. The chemical and structural properties of complex materials at the nanoscale can be directly related to infrared properties of the same regions and validated by characterization obtained on a larger scale using well-established IR spectroscopies[22,23]. We map with sub-nanometre precision the distribution of specific nitrogen- and hydrogen-containing bonding environments and biorelevant molecular moieties across globular-shaped organic grains and nitrogen-containing diffuse OM in Ryugu. The observed nanoscale variations and relationship with surrounding fine-grained minerals shed new light on the origins of these nanoscale organics in Ryugu, offering hints that they were inherited from pre-accretionary, possibly interstellar, precursors before being incorporated into the Ryugu parent body.

3

Results

Previous work has demonstrated the enormous chemical variety and complex morphologies of Ryugu OM[5,12,13,24,25] (Fig. 1). One specifically unique texture of Ryugu OM consists in globular "donut"-shaped or "wormy" regions, where the OM encapsulates mineral grains of various compositions. Similar grains have been observed in other work, named "microglobule" or "interstellar twinkie"[5,19,20,24,26], but investigations by IR techniques, core-loss EELS, and Scanning Transmission X-Ray Microscopy (STXM) yielded inconclusive results concerning their functional chemistry, showing either a high aromaticity of the material by STXM[24], or strong aliphatic bonding by IR[20]. We resolve here these ambiguities by a combined vibrational and core-loss absorption approach, in addition to investigating the enclosed and surrounding phyllosilicate chemistry and textures.

Here we present an in-depth analysis of two such globular grains in lamellae A461-01-FIB01 and C33-FIB03 (Fig. 2, Fig. S1), with several additional hollow microglobules and fragmented globules exhibiting similar functional nano-chemistry occurring throughout our sample set (Fig. S2). In lamella A0461-01-FIB01, we performed detailed low-loss and core-loss EELS analyses on one particularly large (~ 1 µm) donut-shaped grain, where a homogeneous carbon-rich material (carbon 97.3 ± 0.5 at.%, oxygen 2.7 ± 0.4 at.%, other elements below D.L., estimated by core-loss EELS) surrounds a core of phyllosilicates (Fig. 2). The ELNES of the carbon K-edge indicates that the grain belongs to the "highly aromatic" type defined in other work[12,25], where the π^*-peak at ~ 285 eV due to sp^2-carbon dominates other absorption bands such as the "C-O" (ketone/aldehyde) bonding at ~ 286.6 eV. No aliphatic band at ~ 287 eV is visible in the C K-edge spectrum of the donut OM. Nitrogen is slightly enriched in a narrow rim on the outside of the donut OM visible by EDX mapping (Fig. 2g).

EEL spectrum images acquired in the ultra-low loss vibrational range point to a more diverse functional chemistry than visible at the C-K edge only (Fig. 3). Note that the legibility of the VibEELS data is enhanced by scaling the raw data by the square of the energy loss, that is, displaying [intensity × (energy-loss)^2] vs. (energy-loss) (for details see SI). In general, the

4

spectra show the presence of the dominant "Si-O" stretch at around 0.124 – 0.129 eV and a broad spectral band from ~ 0.12 – 0.2 eV (Fig. 3) encompassing multiple overlapping contributions. The typical broader aliphatic C-H$_x$ stretch at ~ 0.37 eV (~ 3000 cm^{-1}) is also present as well as a band at ~ 0.42 – 0.46 eV (~ 3400 – 3700 cm^{-1}) corresponding to the "2.7 µm" O-H stretch feature that has been widely observed by remote sensing on phyllosilicate-rich asteroids such as Ryugu[27,28] or Bennu[29].

We investigated the complex functional chemistry in the VibEEL spectrum of the "donut" OM in more detail (Fig. 3, Tab. S1). Scrutinizing the overall, averaged spectral response of the OM (Fig. 3, spectral component 1), a band at ~ 0.15 eV (~ 1210 cm^{-1}) can be assigned to C-O stretching at 1110 – 1295 cm^{-1} also observed by IR[16]. There is strong absorption in the range ~ 0.165 – 0.18 eV (~ 1330 – 1470 cm^{-1}) dominating the fine structure in this spectral region, likely due to C-H bending, observed at ~ 1375 – 1460 cm^{-1} by IR techniques[16]. Some absorption at ~ 0.2 eV (~ 1610 cm^{-1}) due to sp^2 aromatic carbon is weaker than the C-H bending mode. Therefore, aromatic domains contribute to the signal, as shown in the C-K core-loss spectra, but do not dominate the low-loss regime. The C=O "carbonyl" stretch at ~ 1660 – 1720 cm^{-1} (~ 0.205 – 0.213 eV) is very weak and localizes mostly within the donut OM. Its spatial distribution (Fig. 3, spectral map 1) reveals that small pockets of OM within the pores of the encapsulated phyllosilicates and very fine OM in the surrounding matrix exhibit a similar vibrational signature.

The textures and chemistry of the interior phyllosilicates are clearly different from the surrounding matrix. The interior grains are coarser, enclose a higher volume fraction of pore space, and high-resolution TEM (HRTEM) analyses point to serpentine-type phyllosilicates instead of saponite because of generally smaller lattice spacing values (Fig. 2c)[30,31]. Furthermore, the interior phyllosilicates do not contain any sulfides, whereas there are abundant sulfides such as pyrrhotite in the surrounding more fine-grained matrix (Fig. 2h). This textural difference is also borne out by a detailed vibrational analysis, particularly evident in fine structure differences in the O-H feature: whereas the outside fine-grained component has

5

a less pronounced O-H stretch comprising at least two underlying modes, the interior coarse-grained serpentines yield a much more intense O-H stretch with a single peak at ~ 0.45 eV (Fig. 3). EDX spectra of the interior and outside phyllosilicates also show slightly different Mg/Fe ratios (~ 10.8 in the interior vs. ~ 8.9 in the outside phyllosilicates, excluding any sulfides). Sodium is enriched in the donut-shaped organic grain (Fig. 2i) as well as in other similarly shaped grains observed in our sample set such as the C33-FIB04-grain (Fig. S1).

In addition to large OM grains, diffuse OM in Ryugu is specifically fine-grained and intermingled with phyllosilicates on the nanometre scale. Here, we disentangle the intimate nano-petrographic relationship of this diffuse OM with the phyllosilicates on such an area in lamella A461-01-FIB01 by our combined ELNES-VibEELS approach (Figs. 4+5). The material shows a typical IOM-like C-K edge shape, but no distinct extended fine-structure (Fig. 5b). The surrounding phyllosilicates give a saponite-type signal with bands at 0.06 eV (~ 484 cm^{-1}) and 0.13 eV (Si-O stretch at ~ 1040 cm^{-1}) together with the O-H stretch at ~ 0.45 (spectral component 3 in Fig. 4f). The "pure" OM signal (component 1 in Fig. 4f) shows dominant aliphatic OM with strong C-H_x bending and stretching modes, but almost no O-H stretch, showing that it is not strongly associated with the phyllosilicates. Further fine structure from 0.16 eV (~ 1320 cm^{-1}) to 0.19 eV (~ 1500 cm^{-1}) and a shoulder at 0.2 eV (~ 1610 cm^{-1}) are visible and can be fitted by Gaussian peaks which are distinct from those observed in the donut OM such as slightly stronger C=C and C=O bands (Fig. 4f, Fig. 6, Tab. S1). A C-O stretch as in the donut OM is not observed in this pure OM component (Fig. 6). However, the diffuse OM intermingled with the fine-grained phyllosilicates (component 2, Fig. 4f) shows the Si-O stretch, demonstrating the fine-scale intercalation of the silicates and the OM, but also stronger absorption in the range ~ 0.19 – 0.2 eV likely due to C=C modes. They could also indicate N-H_x bending and C=O stretching in amide bands[32]. This is corroborated by a noisy, but distinct peak at ~ 0.4 eV (~ 3230 cm^{-1} or ~ 3.1 µm) in this diffuse OM component that is also due to N-H_x[14,32]. The aliphatic C-H_x stretch at ~ 0.37 eV is weaker in this material compared to the "pure" OM component.

To evaluate this further, we correlate fitted low-loss bands with core-loss N-K edge spectra of the same nanoscale OM regions (Figs. 5, 6). The C=N (imine or pyridinic N) signal at ~ 398 eV of the N-K ELNES is strong in this material, and further fine structure > 400 eV is visible as well. Statistical analysis of the spectra by blind source separation (bss) algorithms[11] (see SI for details) shows that there are at least two components (Fig. 5g). One component (bss1) is associated with the OM and additional absorption at ~ 401 eV, whereas the other component (bss2) is linked to the phyllosilicates and shows absorption at ~ 402 – 403 eV. ELNES analysis of organonitrogen compounds is complex, but it can be generally stated that the ~ 401 eV absorption could correspond to pyrrolic N, amines, amides, or NH_4^+ ions associated with the diffuse OM[33]. This material therefore relates to a component that is less aliphatic with subtle signs of $N-H_x$ bonding environments. The 402 – 403 eV band of bss2 also matches amine groups, where the transition from mono- to tri-methyl amines and nitrogen coordination shift these bands to higher energies[33,34]. Therefore, the phyllosilicates of bss2 have recorded nitrogen functional groups with less hydrogen and more oxygen, which may finally lead to the formation of amides, probably as the result of fluid processes[32].

Discussion

The variations of the ultra-low energy loss bands observed in our spectra of the donut and diffuse OM point to a richer and more diverse chemical complexity than inferred from ELNES alone. Furthermore, these signals point to processes indicative of interstellar precursors, but also parent-body reactions. At ~ 1330 – 1470 cm^{-1} (~ 0.165 – 0.18 eV), the donut OM shows intense absorption due to C-H bending[16], confirmed by the peak at ~ 0.37 eV. At ~ 1600 cm^{-1} (~ 0.2 eV), sp^2 C=C stretching is typically observed as a major absorption feature in IR spectra of IOM. Although present here, it only appears as a weaker shoulder in the low-loss signal. These observations demonstrate the complementarity of our approach: due to inherently different inelastic cross-sections and scattering physics, the core-loss C-K data shows strong absorption at ~ 285 eV in globular OM and donut-shaped OM regions. This intense π^* peak

7

consistently observed in most amorphous carbon containing materials in turn makes the detection of the aliphatic band at ~ 287 eV very challenging, especially given its known sensitivity to electron dose. The vibrational data on the other hand is particularly sensitive to H-related modes, which are more easily distinguished from the weaker C=C vibrational bands[35].

The C=O double "carbonyl" bonds indicative of, e.g., ketone functional groups, absorb at ~ 0.205 – 0.213 eV (~ 1660 – 1700 cm^{-1}), but are not strongly observed in the donut OM (Fig. 6). The weak shoulder of the donut OM at ~ 1250 cm^{-1} (~ 0.155 eV) also indicates C-O stretching[16] (Fig. 6). This shows that the core-loss 286.6 eV "C-O" feature is dominated by single C-O bonds like in aldehydes in the donut OM. Therefore, whereas the ~ 286.6 eV core-loss signal cannot differentiate between single and double C-O bonding, the low-loss data clearly shows the single C-O predominance, which further underlines the importance and complementarity of a combined low-loss and core-loss approach. Furthermore, the predominance of single C-O bonds demonstrates the aliphatic nature of this pristine material.

In IR studies, the broad "$C-H_x$" feature at around 2900 cm^{-1} (~ 0.37 eV) is known to span several sub-modes, i.e., the CH_3/CH_2 symmetric stretch (2850 cm^{-1}), the CH_2 asymmetric stretch (2925 cm^{-1}) and the CH_3 asymmetric stretch (2960 cm^{-1}) (Tab. S2). In our VibEEL spectra, these modes can be also observed and reveal different local abundances of the CH_2 asymmetric stretch compared to the CH_3 asymmetric stretch (Fig. 6). According to earlier IR work on larger sample volumes, Ryugu OM shows higher CH_2/CH_3 ratios than typical meteoritic materials, implying more aliphatic bonding and longer chains[17,18]. The confirmation of a high abundance of aliphatic chains within the donut OM clearly shows that this aliphatic OM is localized in globular grains and points to an origin in a pre-accretionary, possibly interstellar setting[20]. It has been shown that longer aliphatic chains in extraterrestrial OM are a signature of high pristinity. Fragments of the Tagish Lake carbonaceous chondrite with increasing alteration trends show a decrease in the H/C ratio explained by less aliphatic and more aromatic bonding[36]. Cometary OM assumed to have captured highly pristine organics with little alteration

also shows more intense aliphatic bonding[37]. STXM work by Ito et al. (2022) demonstrates aliphatic bonding in some regions of Ryugu OM[5], but generally, core-loss EELS/STXM work on Ryugu OM rarely shows such aliphatics[12,13,24,25]. This could be explained by the challenge in unambiguously separating the aliphatic peak from the background and more intense features of the C-K spectra, but also due to its high electron beam sensitivity. Whereas core-loss spectra probe highly localized areas, the VibEELS signal is more delocalized, with nanometre-sized areas around the nominal electron beam position (which may be suffering from beam damage) contributing to the recorded intensity. Our low-loss spectra demonstrate the high abundance of aliphatic C-H$_x$ bonding in the Ryugu OM, and shows it stems specifically from unique, highly local features such as the globular donut OM. These observations demonstrate that the two energy loss ranges of this material are complimentary to understand its complex functional chemistry.

The position, width and intensity of the O-H stretch at ~ 0.42 – 0.45 eV depends on whether the O-H is bonded to organic matter (~ 0.41 – 0.42 eV or ~ 3300 – 3400 cm^{-1}) or to cations like Mg in inorganic minerals such as phyllosilicates (~ 0.46 – 0.47 eV or ~ 3700 – 3800 cm^{-1}). Therefore, these bands provide a powerful VibEELS fingerprint to investigate the bonding character of OH-containing materials that are otherwise inaccessible by core-loss EEL spectroscopy. In our VibEEL spectra, the O-H stretch is rarely observed in globular or irregular OM, but more in diffuse OM associated with the Si-O stretch, with careful peak fitting suggesting a mixture of OM and phyllosilicate modes (Fig. S3). The striking difference of the O-H fine structure in the interior and outside phyllosilicates of the donut OM (Fig. 3) indicates different alteration extents of the two regions due to variable microchemical environments, proceeding alteration steps[31], different precursors[30], or space weathering[28]. These observations, only made possible by our small STEM probe geometry, point to an origin of this object in an environment distinct from the surrounding matrix, possibly in a pre-accretionary setting.

9

We conclude that this type of OM has captured a snapshot of pristine, strongly aliphatic material that may be related to the soluble fraction of Ryugu OM due to the observed sodium enrichment (Fig. 2i, Fig. S1c). Bulk analyses on Ryugu SOM have also detected Na-containing organic molecules[38] and there is indication of Na enrichments in Ryugu OM by TEM techniques in other work[31,39]. Furthermore, unique sodium carbonates in Ryugu and Bennu samples demonstrate the existence of highly saline fluids on these asteroids[40,41]. The association of this OM with highly porous serpentine-type phyllosilicates that show a different texture and alteration regime (Fig. 3) underlines this assumption.

We can also draw important conclusions concerning the nano-petrographic texture of diffuse OM and fine-grained phyllosilicates by our combined ELNES/VibEELS approach. The "pure" OM component 1 (Fig. 4f) shows a high abundance of aliphatic chains indicating again a pristine type of OM that is not associated with phyllosilicates. The diffuse OM intermingled with the phyllosilicates, however, shows stronger absorption in the C=C and C=O range as well as indication of $N-H_x$ bonding such as the "0.4 eV" (~ 3230 cm^{-1}) feature (Figs. 4f, Fig. S4c)[16]. We can therefore hypothesize that the more aliphatic diffuse OM was transformed to a more aromatic, C=C and C=O containing material at the interfaces of the fine-grained phyllosilicates, which was also shown to occur on larger scales in chondrites[36]. This process is apparently associated with $N-H_x$ functional groups in this material. A similar process might have played a role in the addition of nitrogen to the donut OM in a thin rim (Fig. 2g).

The observed $N-H_x$ functional groups may originate from ammonia ices that played an important role in these reactions. It is well known that the addition of ammonia increases reaction rates of certain organic synthesis processes such as the formose reaction to polymerize formaldehyde[42,43] or Strecker synthesis to form amino acids[6,8]. By our nanoscale coordinated approach, we therefore show here that these reactions occur at reactive OM-phyllosilicate interfaces within diffuse OM areas. Further proceeding reaction steps of this OM then lead to a more oxygenated and altered component associated with the coarse-grained phyllosilicates (Fig. 5g). Our N-K core-loss data (Fig. 5g) clearly demonstrate the existence of

these amine components with energy absorption > 400 eV associated with the diffuse OM and the phyllosilicates. Ammonia as an important reaction agent could also carry isotopic anomalies formed through UV photodissociation in the solar nebula that may be imprinted onto this OM component[23,32,44,45].

We have shown in this work that the combination of ELNES and VibEELS on the same complex nano-sized organics in Ryugu provides unique complimentary information that is not accessible by other techniques. Globular OM in Ryugu is unambiguously shown to differ from similar nanoglobules in meteorites, and is characterized by aliphatic bonding, sodium enrichments indicative of a soluble organic component, and by specific low-loss fingerprints in its contained phyllosilicates. Diffuse sub-nanometre-scale OM regions also show a strong aliphatic functional chemistry that can be disentangled from a second diffuse OM component. The association of this second diffuse OM component with fine-grained phyllosilicates and N-H_x bonding in some regions point to complex aromatization and nitrogenating reactions, enhanced by an ammonia agent. These characteristics all point to an origin of this OM in a pre-accretionary setting and further complex transformation processes on the Ryugu parent body at reactive phyllosilicate interfaces. Our combined VibEELS approach therefore also sheds new light onto complex alteration processes on carbonaceous asteroids.

References

1   Yada, T. *et al.* Preliminary analysis of the Hayabusa2 samples returned from C-type asteroid Ryugu. *Nature Astronomy* **6**, 214-220 (2022).
2   Nakamura, T. *et al.* Formation and evolution of carbonaceous asteroid Ryugu: Direct evidence from returned samples. *Science*, eabn8671 (2022).
3   Yamaguchi, A. *et al.* Insight into multi-step geological evolution of C-type asteroids from Ryugu particles. *Nature Astronomy* **7**, 398-405 (2023).
4   Hopp, T. *et al.* Ryugu's nucleosynthetic heritage from the outskirts of the Solar System. *Science Advances* **8**, eadd8141 (2022).
5   Ito, M. *et al.* A pristine record of outer Solar System materials from asteroid Ryugu's returned sample. *Nature Astronomy* **6**, 1163-1171 (2022).
6   Pizzarello, S. & Shock, E. Carbonaceous chondrite meteorites: the chronicle of a potential evolutionary path between stars and life. *Origins of Life and Evolution of Biospheres* **47**, 249-260 (2017).

11

7   De Gregorio, B. T. & Engrand, C. Diversity of Complex Organic Matter in Carbonaceous Chondrites, IDPs, and UCAMMs. *Elements* **20**, 24-30 (2024).

8   Martins, Z. The Nitrogen Heterocycle Content of Meteorites and Their Significance for the Origin of Life. *Life* **8**, 28 (2018).

9   Potiszil, C. *et al.* Insights into the formation and evolution of extraterrestrial amino acids from the asteroid Ryugu. *Nature Communications* **14**, 1482 (2023).

10   Naraoka, H. *et al.* Soluble organic molecules in samples of the carbonaceous asteroid (162173) Ryugu. *Science* **379**, eabn9033 (2023).

11   Vollmer, C. *et al.* High-spatial resolution functional chemistry of nitrogen compounds in the observed UK meteorite fall Winchcombe. *Nature Communications* **15**, 778 (2024).

12   De Gregorio, B. *et al.* Variations of organic functional chemistry in carbonaceous matter from the asteroid 162173 Ryugu. *Nature Communications* **15**, 7488 (2024).

13   Stroud, R. M. *et al.* Electron microscopy observations of the diversity of Ryugu organic matter and its relationship to minerals at the micro- to nano-scale. *Meteoritics & Planetary Science* **59**, 2023-2043 (2024).

14   Pilorget, C. *et al.* First compositional analysis of Ryugu samples by the MicrOmega hyperspectral microscope. *Nature Astronomy* **6**, 221-225 (2022).

15   Pilorget, C. *et al.* Phosphorus-rich grains in Ryugu samples with major biochemical potential. *Nature Astronomy* (2024).

16   Kebukawa, Y. *et al.* Infrared absorption spectra from organic matter in the asteroid Ryugu samples: Some unique properties compared to unheated carbonaceous chondrites. *Meteoritics & Planetary Science* **59**, 1845-1858 (2024).

17   Quirico, E. *et al.* Compositional heterogeneity of insoluble organic matter extracted from asteroid Ryugu samples. *Meteoritics & Planetary Science* **59**, 1907-1924 (2024).

18   Dartois, E. *et al.* Chemical composition of carbonaceous asteroid Ryugu from synchrotron spectroscopy in the mid- to far-infrared of Hayabusa2-returned samples. *A&A* **671**, A2 (2023).

19   Phan, V. T. H. *et al.* In situ investigation of an organic micro-globule and its mineralogical context within a Ryugu "sand" grain. *Meteoritics & Planetary Science* **59**, 1983-2001 (2024).

20   Mathurin, J. *et al.* AFM-IR nanospectroscopy of nanoglobule-like particles in Ryugu samples returned by the Hayabusa2 mission. *A&A* **684**, A198 (2024).

21   Krivanek, O. L. *et al.* Vibrational spectroscopy in the electron microscope. *Nature* **514**, 209-212 (2014).

22   Laforet, S. *et al.* Linking Cause and Effect: Nanoscale Vibrational Spectroscopy of Space Weathering from Asteroid Ryugu. *The Astrophysical Journal Letters* **963**, L45 (2024).

23   Vollmer, C. *et al.* Isotopic compositions, nitrogen functional chemistry, and low-loss electron spectroscopy of complex organic aggregates at the nanometer scale in the carbonaceous chondrite Renazzo. *Meteoritics & Planetary Science* **55**, 1293-1319 (2020).

24   Changela, H. G. *et al.* The evolution of organic material on Asteroid 162173 Ryugu and its delivery to Earth. *Nature Communications* **15**, 6165 (2024).

25   Yabuta, H. *et al.* Macromolecular organic matter in samples of the asteroid (162173) Ryugu. *Science* **379**, eabn9057 (2023).

26   Kraver, C. *et al.* An Interstellar Carbonaceous Twinkie in Asteroid Ryugu? *Lunar and planetary science conference* **55**, #2674 (2024).

27   Kitazato, K. *et al.* The surface composition of asteroid 162173 Ryugu from Hayabusa2 near-infrared spectroscopy. *Science* **364**, 272-275 (2019).

28   Le Pivert-Jolivet, T. *et al.* Space weathering record and pristine state of Ryugu samples from MicrOmega spectral analysis. *Nature Astronomy* **7**, 1445-1453 (2023).

29   Lauretta, D. S. *et al.* Asteroid (101955) Bennu in the laboratory: Properties of the sample collected by OSIRIS-REx. *Meteoritics & Planetary Science* **59**, 2453-2486 (2024).

30   Leroux, H. *et al.* Phyllosilicates with embedded Fe-based nanophases in Ryugu and Orgueil. *Meteoritics & Planetary Science* **59**, 1947-1965 (2024).

31   Gainsforth, Z. *et al.* Coevolution of phyllosilicate, carbon, sulfide, and apatite in Ryugu's parent body. *Meteoritics & Planetary Science* **59**, 2073-2096 (2024).

32   Vacher, L. G. *et al.* NH-rich organic compounds from the carbonaceous asteroid (162173) Ryugu: nanoscale spectral and isotopic characterizations. *arxiv.org/abs/2503.11471* (2025).

33   Myneni, S. C. B. Soft X-ray Spectroscopy and Spectromicroscopy Studies of Organic Molecules in the Environment. *Reviews in Mineralogy and Geochemistry* **49**, 485-579 (2002).

34   Cody, G. D. *et al.* Quantitative organic and light-element analysis of comet 81P/Wild 2 particles using C-, N-, and O-μ-XANES. *Meteoritics and Planetary Science* **43**, 353-365 (2008).

35   Rez, P. Is Localized Infrared Spectroscopy Now Possible in the Electron Microscope? *Microscopy and Microanalysis* **20**, 671-677 (2014).

36   Herd, C. D. K. *et al.* Origin and evolution of prebiotic organic matter as inferred from the Tagish Lake meteorite. *Science* **332**, 1304-1307 (2011).

37   Keller, L. P. *et al.* The nature of molecular cloud material in interplanetary dust. *Geochimica et Cosmochimica Acta* **68**, 2577-2589 (2004).

38   Hashiguchi, M. *et al.* The spatial distribution of soluble organic matter and their relationship to minerals in the asteroid (162173) Ryugu. *Earth, Planets and Space* **75**, 73 (2023).

39   Aléon-Toppani, A. *et al.* Correlated IR-SEM-TEM studies of three different grains from Ryugu: From the initial material to post-accretional processes. *Geochimica et Cosmochimica Acta* **371**, 1-30 (2024).

40   Matsumoto, T. *et al.* Sodium carbonates on Ryugu as evidence of highly saline water in the outer Solar System. *Nature Astronomy* **8**, 1536-1543 (2024).

41   McCoy, T. J. *et al.* An evaporite sequence from ancient brine recorded in Bennu samples. *Nature* **637**, 1072-1077 (2025).

42   Kebukawa, Y., Kilcoyne, A. L. D. & Cody, G. D. Exploring the potential formation of organic solids in chondrites and comets through polymerization of interstellar formaldehyde. *The Astrophysical Journal* **771**, 19 (2013).

43   Cody, G. D. *et al.* Establishing a molecular relationship between chondritic and cometary organic solids. *Proceedings of the National Academy of Sciences USA* **108**, 19171-19176 (2011).

44   Pizzarello, S. & Bose, M. The path of reduced nitrogen toward early Earth: the cosmic trail and its solar shortcuts. *The Astrophysical Journal* **814**, 107-114 (2015).

45   Vollmer, C. *et al.* Fluid-induced organic synthesis in the solar nebula recorded in extraterrestrial dust from meteorites. *Proceedings of the National Academy of Sciences* **111**, 15338-15343 (2014).

46   Collins, S. M. *et al.* Functional Group Mapping by Electron Beam Vibrational Spectroscopy from Nanoscale Volumes. *Nano Letters* **20**, 1272-1279 (2020).

Methods

Scanning Electron Microscopy (SEM) / Focused Ion Beam (FIB). Ryugu samples were allocated as polished sections (C0033_04 and C0040_02) and as single particles (A0461, C0396, C0420). Samples from both A and C chamber were studied, but no significant difference was observed within our necessarily limited sample set. The in-depth analysis therefore includes areas extracted indiscriminately from either A or C chamber. Single particles were pressed into high-purity indium foils attached to Al stubs and could then be directly investigated with no further addition of carbon-containing materials such as protection layers or glue. The organic matter can therefore be regarded as "minimally processed",

because no chemicals were used in the preparation of samples and no carbon protection was added. As a result, only the effect of ion and electron beam exposure must be considered.

The general petrography of Ryugu samples was documented using a Hitachi Ethos NX5000 FIB-SEM (3 kV) at the SuperSTEM laboratory. Electron-transparent lamellae were prepared with the Hitachi instrument using advanced FIB preparation protocols, i.e., not exposing lamellae to electrons > 5 kV and using a multi-axis rocking stage to minimize curtaining effects[11]. We generally aimed at OM below the surface and only thinned those regions of interest to electron transparency (< 30 nm in the thinnest regions, and generally < 100 nm across the entire extracted lamellae for 60 kV investigations).

Aberration-corrected Scanning TEM. Electron-transparent lamellae were investigated on a dedicated aberration-corrected monochromated Nion UltraSTEM100MC – Hermes operated at 60 kV to avoid knock-on damage to carbon-based material under ultra-high vacuum conditions to prevent chemical etching of the sample. The instrument is equipped with a cold field emission electron source with a nominal energy spread of ~ 0.3 eV (as measured by the FWHM of the zero-loss peak ZLP). The microscope features an ultra-stable stage, conventional bright-field (BF, 0 - 6.5 mrad angular range in the conditions used for imaging) and high-angle annular-dark-field detectors (HAADF, 90-190 mrad angular range), as well as a Nion IRIS high energy resolution energy loss spectrometer, equipped with a Dectris ELA hybrid pixel direct electron detector. The probe forming optics were adjusted to provide a 0.09 nm probe with a beam convergence of 30 mrad (half-angle), while a collection half-angle of 44 mrad was chosen for EELS analysis. The energy resolution for the carbon and nitrogen K-edge EELS measurements was 0.05 – 0.1 eV, as determined by the position of the monochromator slit position. Spectra from regions of interest were energy-calibrated with respect to the exact position of the ZLP, background subtracted using a decaying power-law function, denoised using Principal Component Analysis, and overlaid against Savitkzy-Golay smoothed lines as a guide to the eye.

The ultra-low energy loss of electrons corresponds to a wavenumber range of ~ 400 – 4000 cm^{-1} (or wavelengths of ~ 2.5 – 25 μm, i.e., the mid-IR). Typical energy resolutions of FT-IR systems are in the 4 cm^{-1} range[17] which translates to about 0.5 meV. The energy resolution of our VibEELS measurements is in the 7 – 9 meV range, which corresponds to a wavenumber resolution of ~ 60 – 70 cm^{-1}. Therefore, although our VibEELS analyses have a lower energy resolution than conventional FT-IR instruments,

they achieve a much better spatial resolution (~ 1 – 2 nm[46]) than AFM-IR instruments or synchrotron-IR setups. Due to delocalization effects, which are wavelength dependent, residual signals can still be detected up to ~ 100 nm at 10 µm (~ 0.13 eV), but this improves to smaller wavelengths. Details about data processing and fitting are provided in the supplementary information.

Conventional 300 kV TEM. After SuperSTEM investigations were completed, lamellae were further analyzed with the aberration-corrected (objective system) ThermoFisher Scientific "Themis" TEM at the University of Münster, using an acceleration voltage of 300 kV, a Fischione Model 6000 HAADF detector, a fast CMOS camera (Ceta 4k x 4k), and a four-quadrant silicon-drift energy-dispersive X-ray (EDX) detector (SuperX technology). We performed conventional BF and HR imaging (usually down to 0.1 nm with the corrected objective system) to document the texture and crystallography of the lamellae with the Gatan Microscopy Suite. EDX spectrum images were acquired in STEM mode (condensor aperture 50 µm, beam convergence 15.7 mrad) using beam currents of about 500-800 pA and analysis times of 100–200 µs/px, with several hundred frames summed up to achieve sufficient counting statistics, quantified using the Velox™ software.
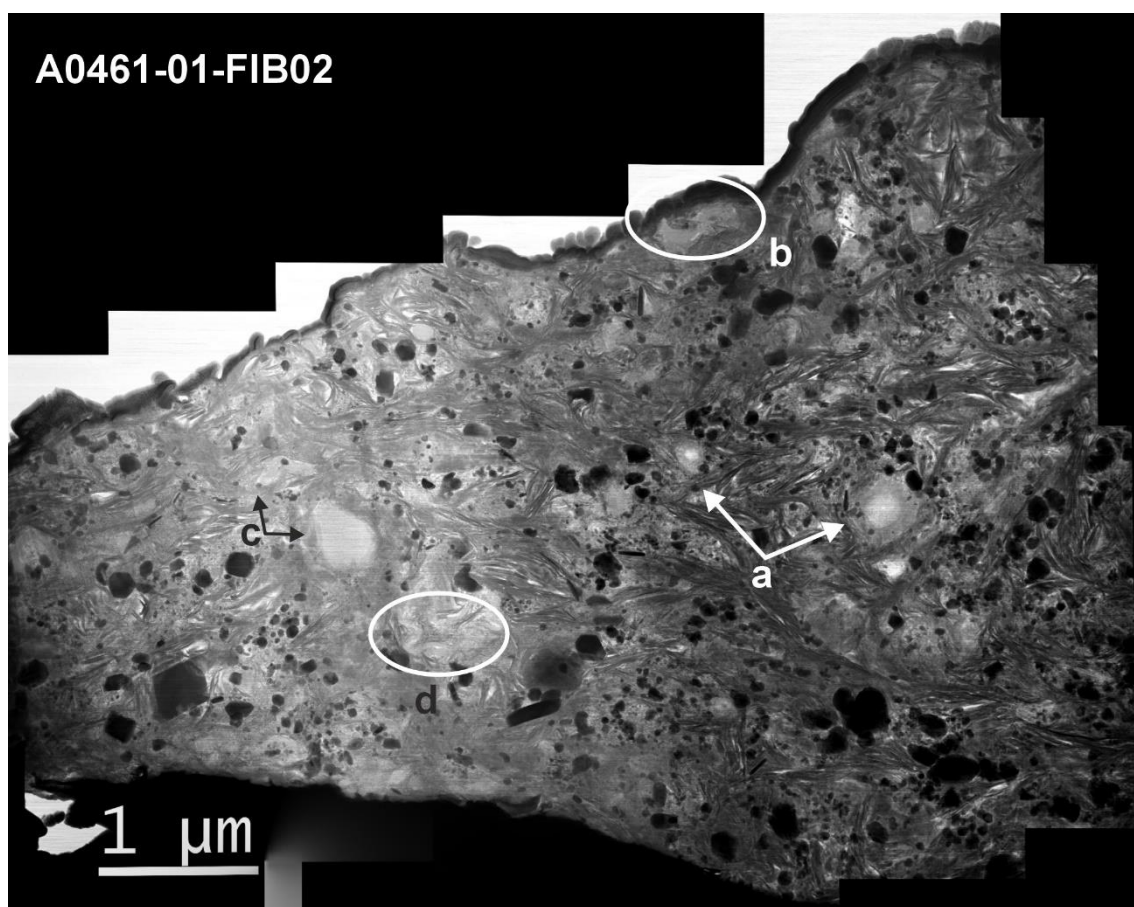
Author contributions. C.V., D.K., and Q.M.R. designed research; C.V., D.K., Q.M.R., and A.B.M. performed research; C.V., J. L., D.K., Q.M.R., and A.B.M. analyzed data; all authors participated in interpretation, C.V. wrote the paper, all authors edited the paper and have approved the submitted version.
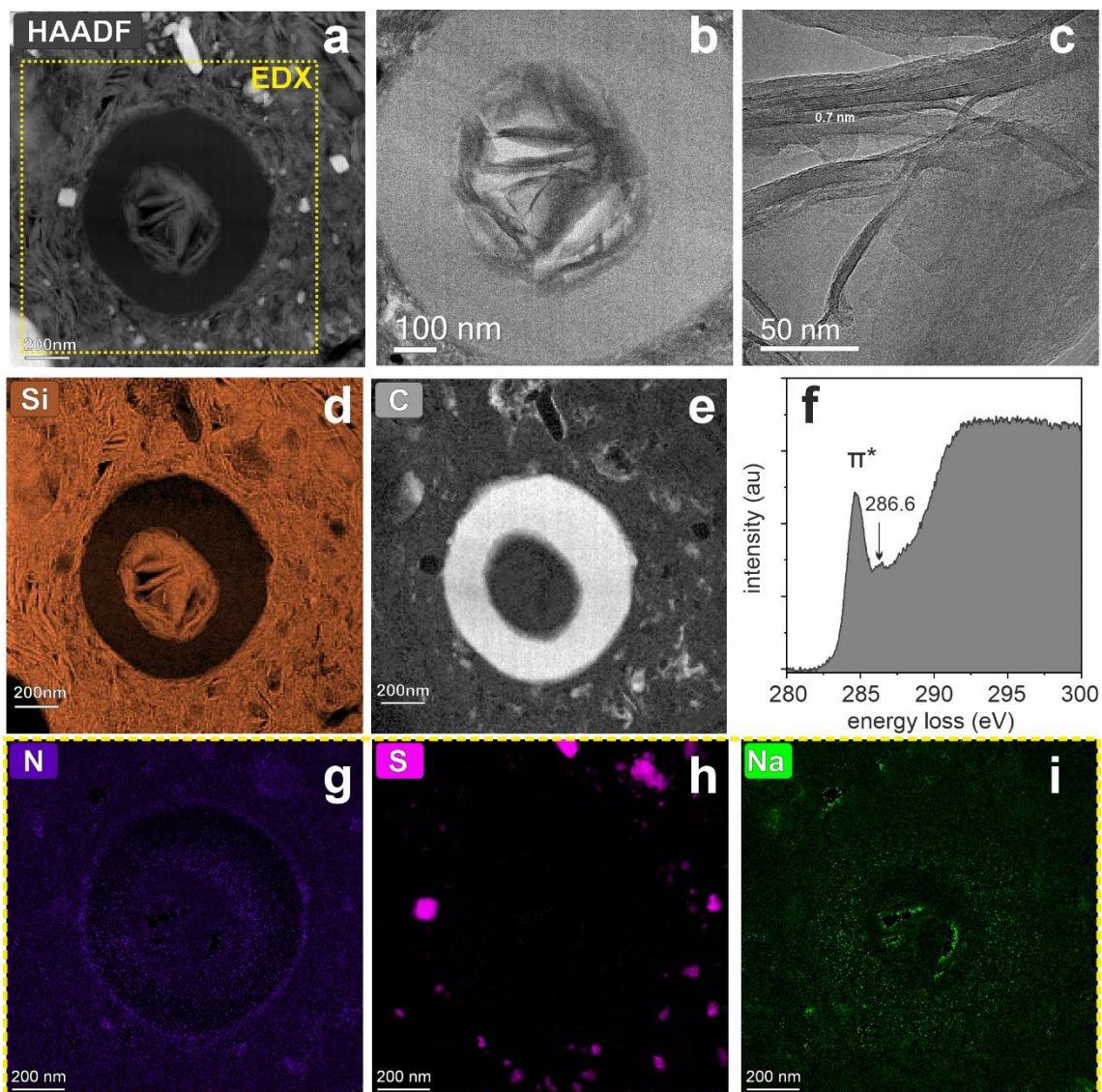
**Competing interests**. The authors declare no competing interests.

Figures

Figure 1. Stitched BF-STEM micrograph of sample A0461-01-FIB02 with the typical observed OM morphologies marked. a – globular OM in various sizes and textures, b – fragmented globular OM, c – irregular OM, and d – diffuse OM between the phyllosilicate layers.

Figure 2. General petrography, chemistry, and texture of the donut OM and its interior and surrounding phyllosilicates. a – HAADF image of the donut OM also showing the different phyllosilicate textures in the interior and the outside. The area of the EDX maps of panels g – i is indicated. b – BF image showing the smooth contrast of the donut OM with no internal variations. Inner coarse-grained phyllosilicates have high porosity. c – HR image of the inner phyllosilicates with the characteristic 0.7 nm d spacing of serpentines. d – Silicon map (60 kV STEM-EELS), e – Carbon map (60 kV STEM-EELS). f – Extracted Carbon K-edge spectrum of the donut OM with strong "285 eV" π^* absorption due to sp^2 carbon and minor "C-O" bonding at ~ 286.6 eV. g – Nitrogen map (300 kV STEM-EDX) showing an enhanced N content on the outside of the donut OM, h – Sulfur map (300 kV STEM-EDX) demonstrating the lack of sulfides in the interior phyllosilicates, i – Sodium map (300 kV STEM-EDX) showing the slight Na enhancement of the donut OM.
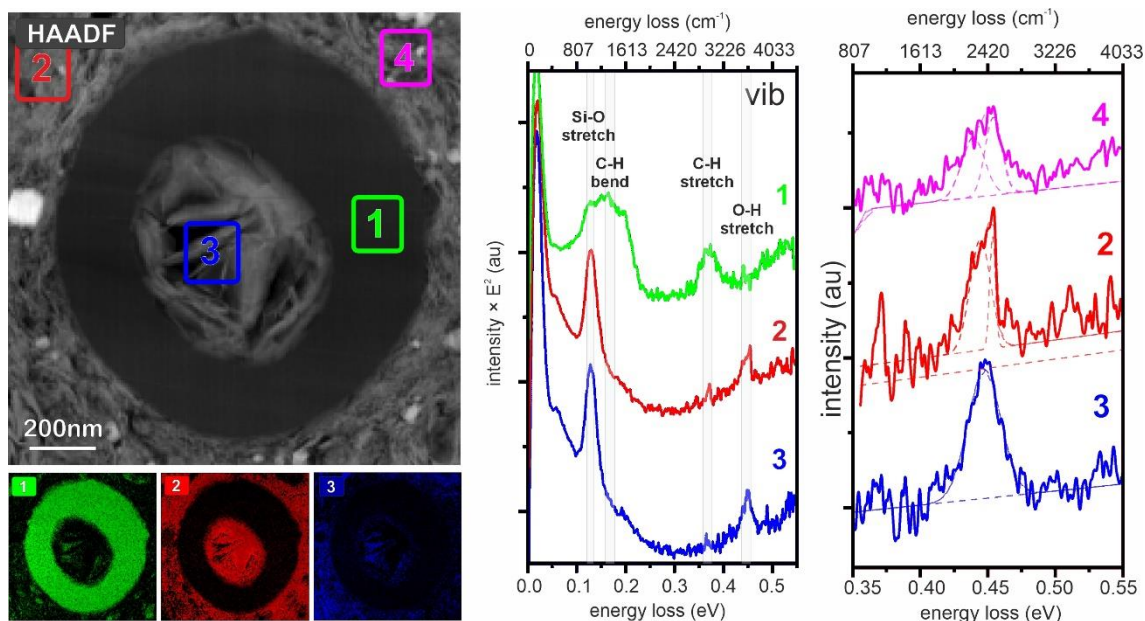
Figure 3. Vibrational EEL spectra with major bands marked and extracted component maps of the different donut OM regions. *Upper left* – STEM-HAADF micrograph of the donut OM. *Middle* – Three extracted components and respective VibEEL spectra of (1) the OM, (2) the outer matrix, and (3) the interior phyllosilicates. *Right* – Detailed vibrational EELS analysis of the O-H stretch around the donut OM. Whereas the interior coarse-grained phyllosilicates are characterized by a single, strong O-H stretch, the outside, finer-grained matrix comprises two different less-pronounced modes due to mixed organic-inorganic OH modes. The vibrational EELS data (scaled by E^2) was fitted with Gaussian curves after principal component analysis (PCA).
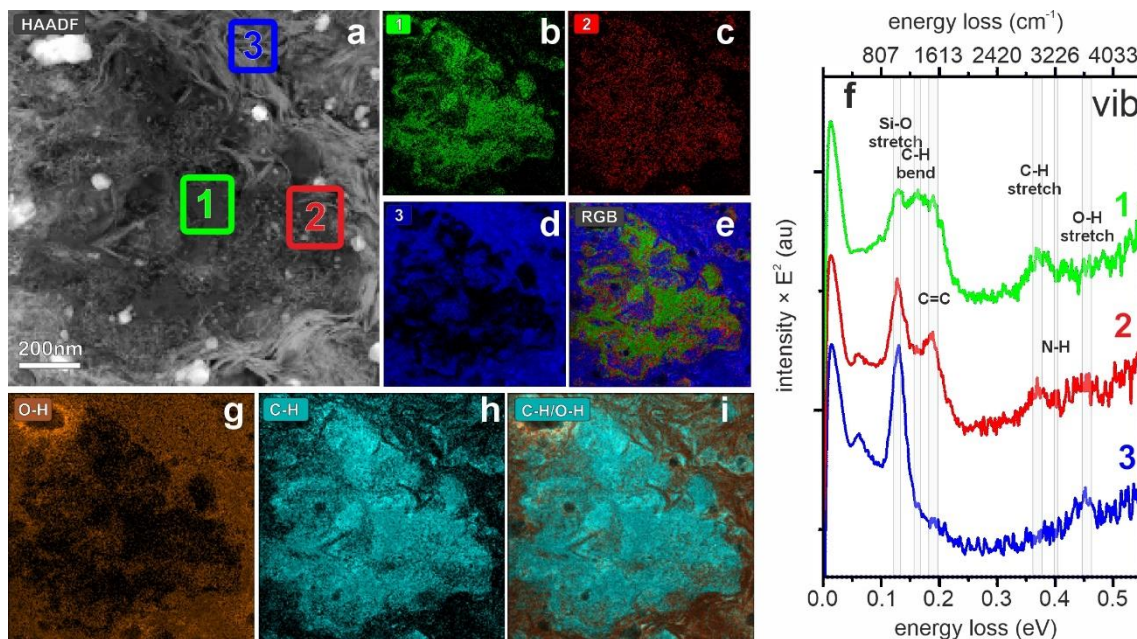
Figure 4. Vibrational EELS of the diffuse N-containing OM in lamella A0461-01-FIB01 with extracted maps and spectra. a – HAADF overview of the diffuse OM area with three different regions marked. b – Extracted map of the "pure" OM component (1). c – Extracted map of the diffuse OM intermingled with fine phyllosilicates (2). d – Extracted map of the surrounding phyllosilicates (3). e – RGB colored overlay map of the three components. f – Vibrational EEL spectra of the OM regions marked in (a). The intermingled OM-fine phyllosilicates (2) show an additional faint band at ~ 0.4 eV. g – Map of the O-H stretch showing mainly phyllosilicates. h – Map of the C-H stretch showing mainly diffuse OM. i – Combined map of the two components. The maps were produced by multi-linear least squares fitting of the spectra in panel f, and for energy ranges b – d 0.05 – 0.25 eV and g,h 0.3 – 0.5 eV, respectively. For the maps g,h only the spectra from regions 1 and 3 were used.
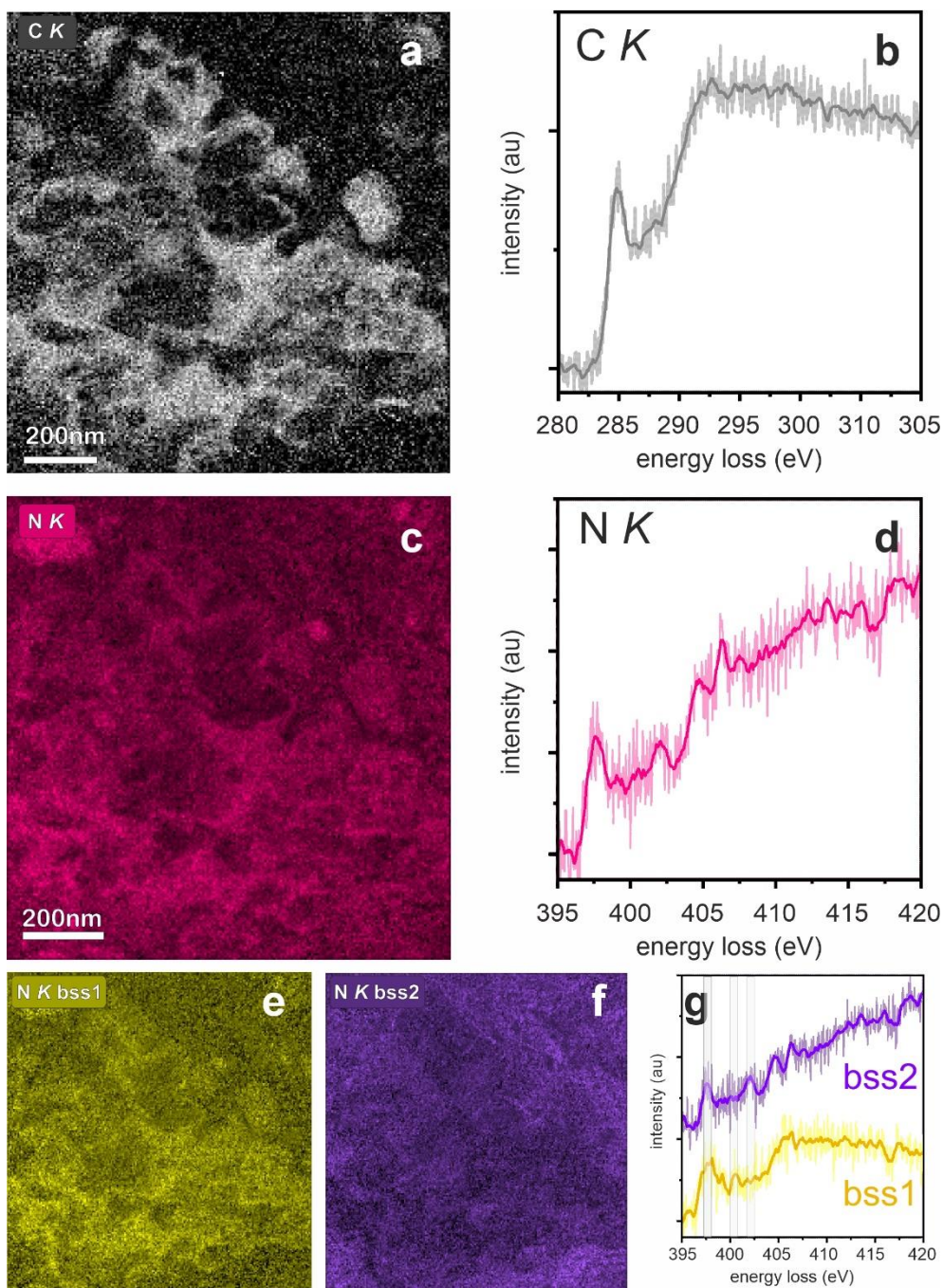
Figure 5. Core-loss EELS of the diffuse N-containing OM in lamella A0461-01-FIB01 with extracted maps and spectra and blind source separation analysis. a – Carbon STEM-EELS map. b – Extracted Carbon K-edge spectrum of the diffuse OM showing the "285 eV" π^* absorption but barely any further fine structure. c – Nitrogen STEM-EELS map. d – Extracted Nitrogen K-edge spectrum of the diffuse OM showing an imine band below 400 eV, but also absorption in the 401 – 403 eV range indicative of N-H$_x$ moieties. e, f – BSS loadings of the N-K spectrum associated mainly with the diffuse OM (bss1) and the phyllosilicates (bss2) and corresponding BSS components (g) showing different bands above 400 eV due to amine/amide bonding (see text and SI for details).
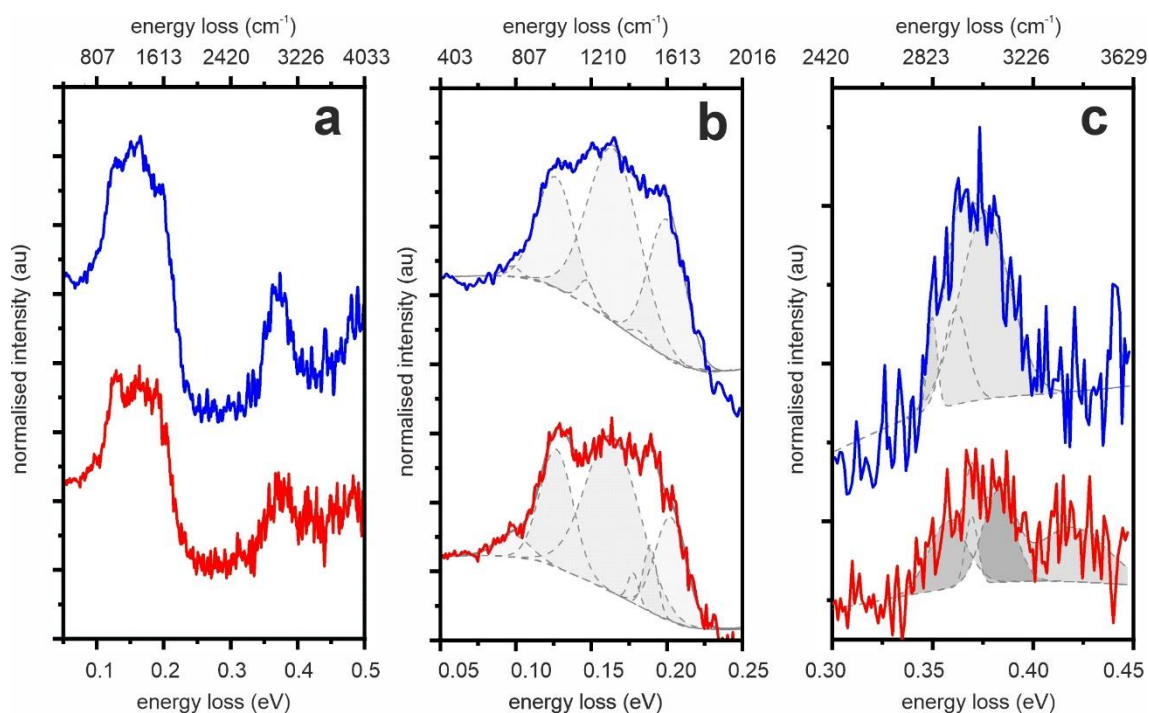
Figure 6. Detailed analysis of the VibEEL spectra of the donut and the diffuse OM. a – Whole range representative average spectra of the donut OM (blue) and the diffuse OM (red). b – Analysis of the main OM features in the energy range 0.1 – 0.2 eV showing several components that can be fitted with Gaussians and demonstrate that the two OM types contain different and complex bonding environments. c – The broad CH_x stretch feature can be fitted by the symmetric and asymmetric vibrational modes (Supplementary Table S2).

Supplementary information

Additional vibrational EELS analysis

The vibrational spectra of the different areas studied here reveal a rich and complex fine structure (Tab. S1). Ryugu samples are mainly CI-type materials and composed of phyllosilicates such as saponite and serpentine leading to a dominant Si-O stretching mode at around 1000 cm^{-1} (~ 10 µm) in all samples[1-3]. This IR band is strong in untreated Ryugu samples, but absent in demineralized and extracted IOM[4-6]. In our VibEEL spectra, this mode occurs at ~ 0.124 - 0.129 eV (Tab. S1) (~ 1000 – 1040 cm^{-1}). Clay-type phyllosilicates such as saponite usually give an IR signal > 1000 cm^{-1}, whereas serpentine-type phyllosilicates are usually < 1000 cm^{-1} [5], which supports the predominance of saponite-type clays over serpentine in Ryugu. This is in further agreement with Leroux *et al.* (2024)[7] who investigated the mineralogy of the coarse- and fine-grained phyllosilicates in Ryugu and found that the fine-grained component is more likely composed of saponite-type clays evolving from a different precursor such as amorphous silicates, whereas the coarse-grained, more serpentine-type phyllosilicates originate from anhydrous precursors such as olivine and pyroxene.

Towards the far-IR (<1000 cm^{-1}, >10 µm), additional fine structure is mainly due to minerals in the Ryugu matrix associated with the OM. A band at ~ 0.06 eV (~ 484 cm^{-1}) occurs together with the Si-O stretch in saponite-type clays (see Fig. 11 in Dartois *et al.*, 2023[5]), probably due to silicate vibrations also known from astrophysics as the "22 µm feature"[8]. Magnetite is abundant in Ryugu matrix[9] and observed bands at 0.04 eV (360 cm^{-1}) and 0.07 eV (570 cm^{-1}) (Fig. S4c) in one VibEEL spectrum of magnetite in our Ryugu samples fit to literature values of magnetite in the far-IR[5]. Sulfides such as pyrrhotite are another major mineral phase within the matrix of Ryugu and are related to a band at ~ 270 cm^{-1} (~ 0.03 eV), which is usually not measured with conventional IR spectrometers due to the limited energy range. This extremely low energy loss band is difficult detect on the tail of the zero-loss peak, but is present in some of our spectra, especially in the thinnest areas of the extracted lamellae wherein the effects of zero-loss-tail broadening are less restrictive.

EELS Data processing

EELS spectrum images were denoised using Principal Component Analysis (PCA) as implemented in the Gatan GMS3.6 software suite[10]. The use of a hybrid-pixel electron detector optimized for low-beam-energy electron energy loss spectroscopy (EELS) provides major advantages, such as low noise and high detection quantum efficiency, even in low dose conditions. The Poisson-nature of any remaining noise in the spectra lends itself to efficient denoising using PCA methods[11].

VibEELS spectra are presented after scaling by the square of the energy loss, that is, displaying (intensity × (energy-loss E)^2) vs. (energy-loss E), to account for the energy-dependent occupancy of phonon excitations with a Bose-Einstein model in the very low energy loss limit. This scaling by E^2 gives a better visual match and by extension aids comparison with IR data. The VibEELS spectra were fitted by Gaussian functions in OriginLab. The number of components was selected to correspond to the expected number of spectral bands in IR, with no further restriction to the fit.

The VibEELS spectral maps in Figs. 3, 5 were generated by multi-linear least-squares fitting of internal reference spectra and energy ranges selected from regions of interest in the spectrum image, as implemented in the Gatan GMS3.6 platform[10].

The EELS core-loss chemical maps (Figs. 3, 6) were generated by integrating at each point of the denoised spectrum images the spectrum intensity over an ~ 30 eV window above the edge onsets after background subtraction using a power law model. The N-K EELS data of the diffuse area (Fig. 5) were statistically analyzed using blind source separation (BSS) as implemented in the Hyperspy code. The method allows for the unmixing of original source signals from their intermixed observations[12,13].

Supplementary References

1   Nakamura, T. *et al.* Formation and evolution of carbonaceous asteroid Ryugu: Direct evidence from returned samples. *Science*, eabn8671 (2022).

2   Yada, T. *et al.* Preliminary analysis of the Hayabusa2 samples returned from C-type asteroid Ryugu. *Nature Astronomy* **6**, 214-220 (2022).

3   Yokoyama, T. *et al.* Samples returned from the asteroid Ryugu are similar to Ivuna-type carbonaceous meteorites. *Science* **379**, eabn7850 (2023).

4   Kebukawa, Y. *et al.* Infrared absorption spectra from organic matter in the asteroid Ryugu samples: Some unique properties compared to unheated carbonaceous chondrites. *Meteoritics & Planetary Science* **59**, 1845-1858 (2024).

5   Dartois, E. *et al.* Chemical composition of carbonaceous asteroid Ryugu from synchrotron spectroscopy in the mid- to far-infrared of Hayabusa2-returned samples. *A&A* **671**, A2 (2023).

6   Quirico, E. *et al.* Compositional heterogeneity of insoluble organic matter extracted from asteroid Ryugu samples. *Meteoritics & Planetary Science* **59**, 1907-1924 (2024).

7   Leroux, H. *et al.* Phyllosilicates with embedded Fe-based nanophases in Ryugu and Orgueil. *Meteoritics & Planetary Science* **59**, 1947-1965 (2024).

8   Chan, K.-W. & Onaka, T. A Broad 22 Micron Emission Feature in the Carina Nebula H II Region*. *The Astrophysical Journal* **533**, L33 (2000).

9   Dobrică, E. *et al.* Nonequilibrium spherulitic magnetite in the Ryugu samples. *Geochimica et Cosmochimica Acta* **346**, 65-75 (2023).

10   Lucas, G., Burdet, P., Cantoni, M. & Hébert, C. Multivariate statistical analysis as a tool for the segmentation of 3D spectral data. *Micron* **52-53**, 49-56 (2013).

11   Haberfehlner, G. *et al.* Benefits of direct electron detection and PCA for EELS investigation of organic photovoltaics materials. *Micron* **140**, 102981 (2021).

12   Bi, Y., Lu, Y., Long, Z., Zhu, C. & Liu, Y. in *Tensors for Data Processing* (ed Yipeng Liu) 1-30 (Academic Press, 2022).

13   Vollmer, C. *et al.* High-spatial resolution functional chemistry of nitrogen compounds in the observed UK meteorite fall Winchcombe. *Nature Communications* **15**, 778 (2024).

Additional Figures
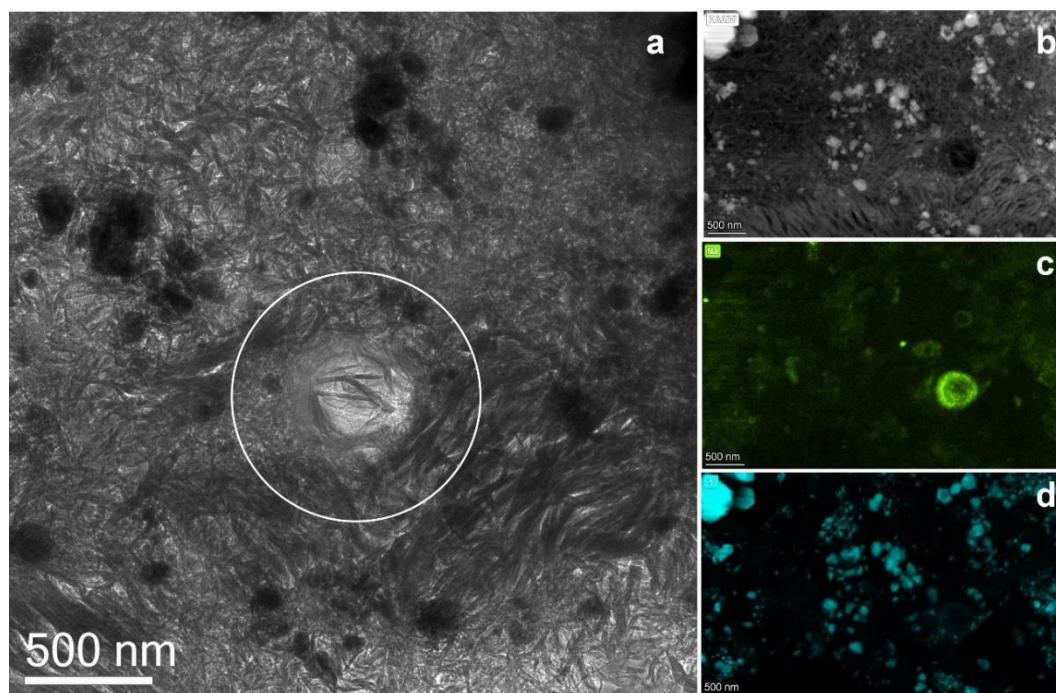
Figure S1. TEM micrographs and STEM-EDX maps of a "donut" OM grain in sample C33_FIB03 a – overview BF-TEM image of the donut (encircled), b – overview HAADF-STEM image, c – STEM-EDX map of sodium in the same area as panel b. d – STEM-EDX map of sulfur in the same area showing the lack of any sulfides in the second donut OM grain.
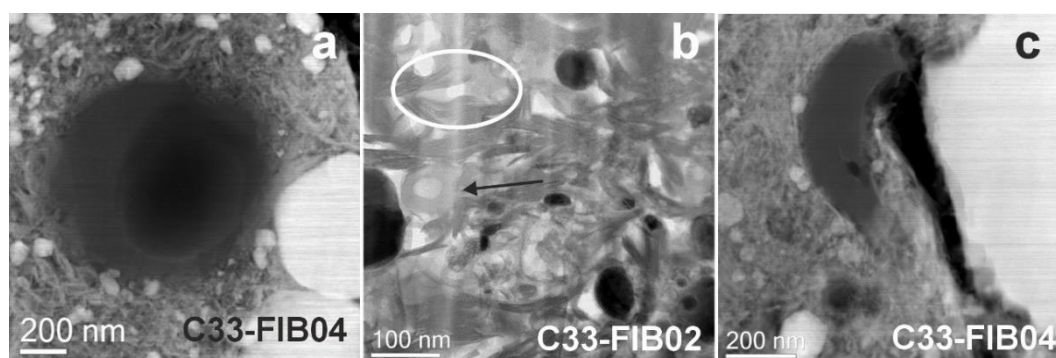
Figure S2. STEM micrographs of morphological OM details. a – HAADF-STEM- image of a hollow globule in sample C33-FIB04, b – BF-STEM image of a miniglobule (arrow-marked) and diffuse OM within the phyllosilicates (encircled) in C33-FIB02, c – HAADF-STEM image of a fragment of a globular OM grain in C33-FIB04.

26
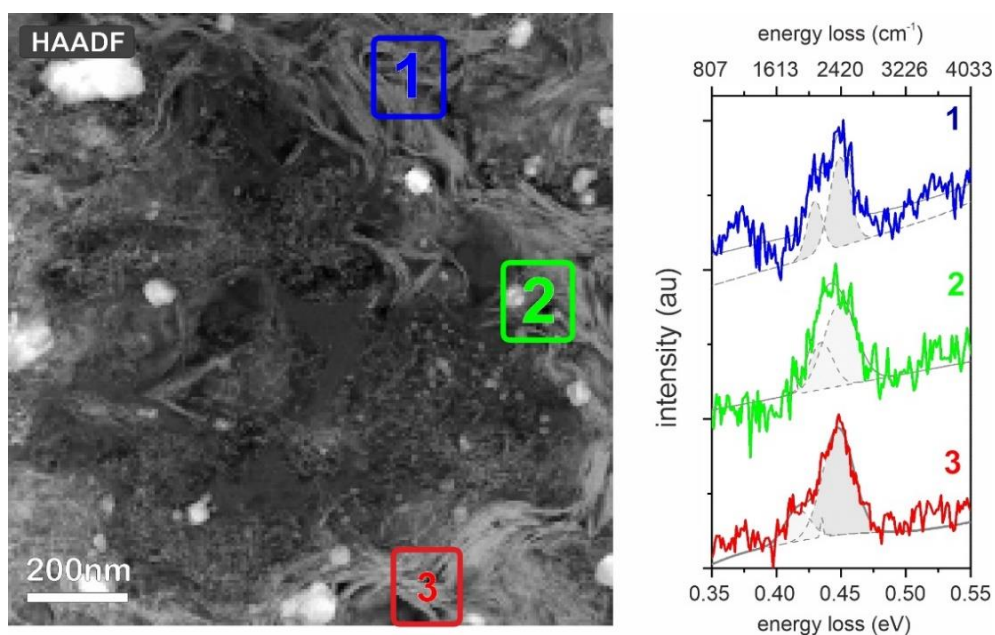
Figure S3. VibEELS analysis of the phyllosilicates surrounding the diffuse N-containing OM area in lamella A461-01-FIB01. HAADF-STEM overview image with three different ROI indicated for extracted spectra and spectral analysis using fitting with Gaussian functions (see also Supplementary Table S3). The fine-grained matrix comprises three different modes due to mixed organic-inorganic OH bonding and possibly overlapping NH_x bonds towards ~ 0.4 eV.
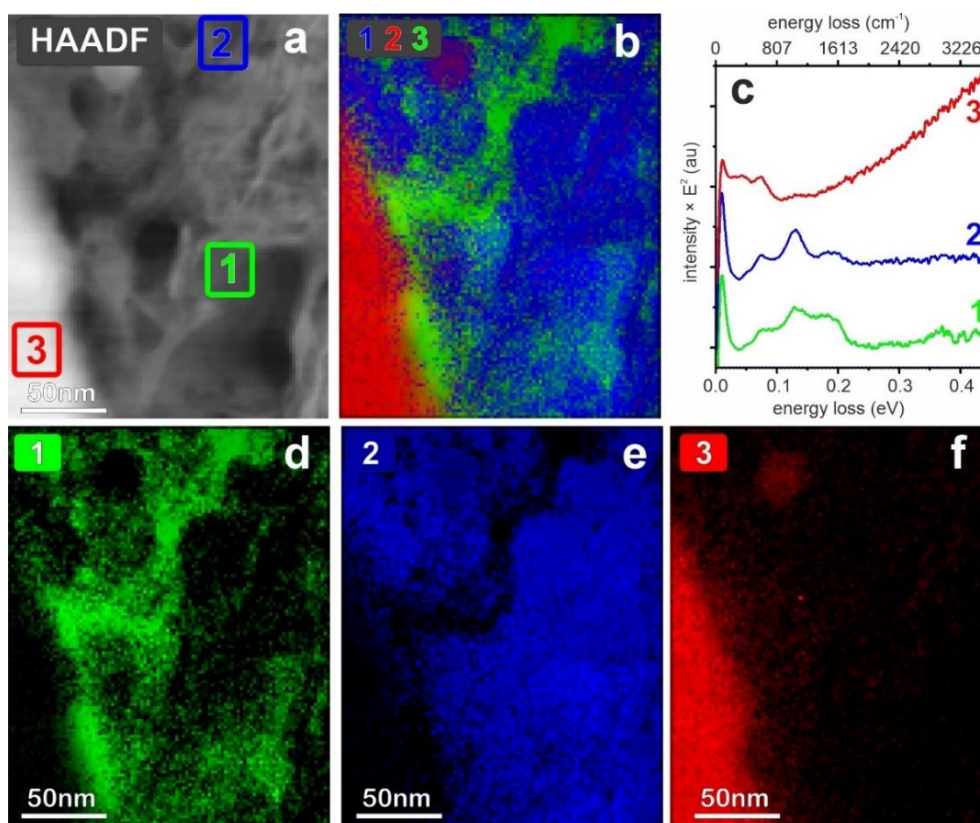
Figure S4. Vibrational EELS of a second diffuse N-containing OM area and associated minerals in lamella C40-FIB05. a – HAADF-STEM overview image with three different ROIs indicated for extracted spectra and respective maps, b – RGB map of the three different components. c – VibEEL spectra of the three different components, with the diffuse OM (1) showing a clear band at ~ 0.4 eV. d – Extracted distribution map of the diffuse OM (1), e – Extracted distribution map of the phyllosilicates (2), f – Extracted distribution map of the magnetite in the lower left (3).

Additional Tables

Supplementary Table S1: Organic matter VibEELS peak assignments

Donut			Diffuse		
eV	cm^{-1}	Possible assignment	eV	cm^{-1}	Possible assignment
0.126	1016	Si-O stretch (saponite)	0.127	1024	Si-O stretch (saponite)
0.147	1185	**C-O stretch**	-	-	-
0.165	1330	C-H bend	0.164	1323	C-H bend
0.182	1468	C-H bend	0.178	1436	C-H bend
-	-	-	0.189	1524	**N-H bend?**
0.200	1613	C=C, C=O	0.202	1629	C=C, C=O
0.372	3000	C-H$_x$	0.372	3000	C-H$_x$

Supplementary Table S2: Organic matter VibEELS analysis of the C-H$_x$ peak

Donut			Diffuse		
eV	cm^{-1}	Possible assignment	eV	cm^{-1}	Possible assignment
0.350	2823	CH$_3$/CH$_2$ symmetric stretch	0.357	2879	CH$_3$/CH$_2$ symmetric stretch
0.361	2912	CH$_2$ asymmetric stretch	0.369	2976	CH$_2$ asymmetric stretch
0.376	3033	CH$_3$ asymmetric stretch	0.383	3089	CH$_3$ asymmetric stretch

Supplementary Table S3: Organic matter VibEELS analysis of the O-H feature

Area 1			Area 2			Area 3		
eV	cm^{-1}	Possible assignment	eV	cm^{-1}	Possible assignment	eV	cm^{-1}	Possible assignment
-	-	-	0.414	2995	N-H$_x$?	0.416	2980	N-H$_x$?
0.429	2890	O-H in OM	0.434	2857	O-H in OM	0.435	2850	O-H in OM
0.449	2761	Inorganic O-H	0.449	2761	Inorganic O-H	0.447	2774	Inorganic O-H